Transformation of taxol-stabilized microtubules into inverted tubulin tubules triggered by a tubulin conformation switch

Miguel A. Ojeda-Lopez[#1,2], **Daniel J. Needleman**[#1,3], **Chaeyeon Song**[#4], **Avi Ginsburg**[5], **Phillip A. Kohl**[6], **Youli Li**[6], **Herbert P. Miller**[7], **Leslie Wilson**[7], **Uri Raviv**[5], **Myung Chul Choi**[4], and **Cyrus R. Safinya**[1,*]

[1]Materials Department, Physics Department, Molecular, Cellular, and Developmental Biology Department, University of California, Santa Barbara, CA 93106, USA

[4]Department of Bio and Brain Engineering, Korea Advanced Institute of Science and Technology (KAIST), Daejeon, Republic of Korea

[5]Institute of Chemistry, The Hebrew University of Jerusalem, Edmond J. Safra Campus, Givat Ram, 91904 Jerusalem, Israel

[6]Materials Research Laboratory, University of California, Santa Barbara, CA 93106, USA

[7]Molecular, Cellular, & Developmental Biology Department & Neuroscience Research Institute, University of California, Santa Barbara, CA 93106, USA

[#] These authors contributed equally to this work.

Abstract

Bundles of taxol-stabilized microtubules (MTs) – hollow tubules comprised of assembled αβ-tubulin heterodimers – spontaneously assemble above a critical concentration of tetravalent spermine and are stable over long times at room temperature. Here we report that at concentrations of spermine several-fold higher the MT bundles (B_{MT}) quickly become unstable and undergo a shape transformation to bundles of inverted tubulin tubules (B_{ITT}), the outside surface of which corresponds to the inner surface of the B_{MT} tubules. Using transmission electron microscopy and synchrotron small-angle x-ray scattering, we quantitatively determined both the nature of the B_{MT} to B_{ITT} transformation pathway, which results from a spermine-triggered conformation switch from straight to curved in the constituent taxol-stabilized tubulin oligomers, and the structure of

[*]Correspondence and requests for materials should be addressed to C.R.S. safinya@mrl.ucsb.edu.
[2]Present address: Universidad Autonoma de San Luis Potosí, Instituto de Física, Zona Universitaria 78290, San Luis Potosí, México.
[3]Present address: School of Engineering and Applied Science; Molecular and Cellular Biology; and FAS Center for Systems Biology, Harvard University, Cambridge, MA 02138, USA.

Author Manuscript Author Manuscript Author Manuscript Author Manuscript

the B_{ITT} phase, which is formed of tubules of helical tubulin oligomers. Inverted tubulin tubules provide a platform for studies requiring exposure and availability of the inside, luminal surface of MTs to MT-targeted-drugs and MT-associated-proteins.

Proteins often undergo abrupt structural transitions, which enables their functions. These discrete conformational changes underlie the exquisite control and sensitivity of biological organisms. Examples include pH sensitive flagella and molecular motor ATPases such as kinesin and myosin motors undergoing conformational changes with altered states leading to discriminating binding affinities for $ADP + P_i$ and ATP[1,2]. In contrast to the (switch like) discrete conformational states of proteins, many other biomacromolecules undergo continuous shape changes. For example, lipids may form spherical and cylindrical micelles, bilayers, or other assemblies, as variations in their local environment (pH, ionic strength, addition of co-lipids) continuously change the lipid's shape[3–7].

In our studies we used proteins, which harness discrete shape remodeling specificity used in biology, as self-assembling building blocks. These "genetically preprogrammed" nanomaterials were found to be susceptible to molecularly triggered disassembly and simultaneous reassembly and emergence of new structure. This new paradigm for self-assembly is distinct from those employed previously where the complementary binding (*i.e.* recognition specificity) present in proteins, DNA, and RNA is used to construct specific contact between sub-units, allowing assembly into predictable yet relatively stable structures[8–11].

The building blocks in our study were αβ-tubulin heterodimers, which exist in two distinct conformations with the transition between these two states controlled by GTP hydrolysis[12–14]. Protofilaments (PFs) – head-to-tail assemblies of αβ-tubulin heterodimers αβ adapt straight and curved conformations for the GTP-tubulin and GDP-tubulin conformations, respectively. The assembled microtubule (MT) (Fig. 1a) consisting, on average, of 13 straight PFs is stabilized by lateral PF-PF interactions. (Tubulin's distinct conformations underlie the broad range of cellular activities of tubulin and polymerized tubulin (i.e. MTs) which include imparting cell shape, as tracks for organelle transport, and as building blocks of dynamical spindles[1,2].) MT disassembly (*e.g.*, during dynamic instability) occurs when the layer of GTP containing β-subunits at the MT growing end is lost and when MTs depolymerize the protofilaments peel off as highly bent GDP-tubulin oligomers[15,12]. The cancer chemotherapy drug taxol maintains the straight conformation for GDP-PFs (post hydrolysis) upon binding to the β-subunit facing the inner lumen[16–19]. Taxol stabilizes the straight conformation for GDP-PFs by raising the energy barrier and thus preventing the straight-to-curved transition over very long periods of time, on the order of many weeks to months (depending on the molar ratio of taxol to tubulin dimers)[20,21]. Indeed, elegant AFM studies, at the single PF level, of taxol-stabilized straight and ring-like GDP-PFs show that taxol slows down the straight to curved transition of GDP-PFs[20].

In a previous study it was found that taxol-stabilized MTs can be induced to assemble into hexagonally packed bundles, the B_{MT} phase, above a critical concentration of tetravalent spermine (4+) (Fig. 1b)[22]. The origin of the assembly is counterion-induced electrostatic attractions[23,24] between spermine coated MTs[25]. Spermine is a biological polyamine present

at millimolar concentrations in eukaryotic cells, and, as an efficient counterion to anionic cytoskeletal filaments (e.g. F-actin and MTs), may have a regulatory role on the architecture of cytoskeletal networks in cells[26].

In the current study we find that while the spermine-induced MT bundled structure (Fig. 1b) is stable for long periods at concentrations just above the critical bundling concentration (C_c) at room temperature[22], at higher concentrations (several times C_c), spermine triggers bundle disassembly by inducing a straight to curved transition and outwardly peeling of taxol-containing protofilaments within bundles (Fig. 1c; see also Fig. 3 a–d and Supplementary Fig. S1). Concurrently, the presence of counterion spermine leads to assembly of curved protofilaments (c-PFs) into a tubular structure (Fig. 1d), which as transmission electron microscopy (TEM) shows, is distinct from tubules formed by GDP-PFs in the straight conformation. Furthermore, quantitative analysis of synchrotron small-angle-x-ray-scattering (SAXS) data reveals that the single-walled tubules consist of helical PFs with the tubules ordered into hexagonal bundles. Thus, as TEM and SAXS show PFs in the curved and straight conformations both form arrays of hollow nanometer scale tubules, but because of the inside-out curving of PFs during the peeling process, the surface which is on the *inside* of the B_{MT} tubes (Fig. 1b) is *outside* on the new array of tubules, which we refer to as a bundle phase of inverted tubulin tubules (B_{ITT}) (Fig. 1d). Our discovery is consistent with the hypothesis that spermine controls the energy barrier between the straight and curved conformations of taxol-stabilized GDP-PFs, and as time-dependent SAXS shows, lowers the barrier with increasing concentrations.

Tubulin may be induced to form a variety of alternative structures in the presence of polycations and divalent cations[27–33]. Double-walled structures have been observed to result from tubulin in reassembly buffer (containing GTP) at 37 °C, which contains cationic DEAE-dextran[27,28,30] or a range of synthetic polycations[29]. TEM shows that the double-walled structure consists of tubulin rings wrapped around a microtubule core[27–30]. Because more recent cryo-TEM studies have shown that tubulin rings have a natural inside-out curvature[15,12] then it follows that the rings in the doubled walled structures of the earlier work[27–30] also have the same orientation. More recent cryo-EM studies of Mn^{2+} induced assembly of GDP-tubulin at 37 °C has revealed the formation of a different type of double-layered tubes with PFs aligned approximately perpendicular to the tube axis for both layers[33]. Cryo-EM reconstruction at 1.2 nm resolution shows that the outer wall consists of a tight one-start helix of 32 tubulin monomers with an inside-out orientation of the PF. The orientation and helical nature of the outer wall of these double-walled tubes appear to be quite similar to the single-walled inverted tubulin tubules (ITTs) described here.

In the work described here we show in some detail, using TEM and SAXS, the pathway of inversion of bundles of taxol-stabilized-MTs into bundles of *single*-walled tubules. The discovery of spermine triggered depolymerization of MTs is highly surprising given the known stabilizing effects of taxol on MTs against a variety of destabilizing conditions including cold[16–19]. Furthermore, while the depolymerization of taxol-stabilized MTs appears to have specificity (e.g., spermidine, a closely related oligoamine, does not depolymerize taxol-stabilized MTs on the time scale of 2 to 3 weeks) the formation of a

variety of double walled structures from tubulin,[27–30,33] mixed with a range of cationic macromolecules or divalent ions, appears to be non-specific.

The transition from the B_{MT} to B_{ITT} phase is strongly temperature dependent varying between days to hours in going from room temperature (RT) to 0 °C with spermine concentrations in the millimolar range. A TEM micrograph of a relatively large bundle of taxol-stabilized MTs formed in the presence of 10 mM spermine (well above the critical bundling concentration C_c of 1.5 ± 1 mM) can be seen in Fig. 2a. (The inset to Fig. 2a shows the individual taxol-stabilized MTs at a lower magnification (18.18 μM tubulin, taxol/ tubulin molar ratio = 0.55) in the absence of spermine.) For these preparations the B_{MT} phase is the dominant component for periods less than 10 days at RT after which coexistence with the new B_{ITT} phase is observed. At higher spermine concentrations (15 mM) at RT, the B_{MT} phase is progressively replaced by the new B_{ITT} phase after 10 days. A large bundle of the B_{ITT} phase 10 days after addition of 25 mM spermine to MTs at RT is shown in the TEM micrograph in Fig. 2b. A high magnification example of a small bundle of the B_{ITT} phase prepared under the same conditions is shown in Fig. 2c. The transition from the B_{MT} phase to this new phase is observed to occur on much shorter timescales at 4 °C where Fig. 2d shows an example of the B_{ITT} phase 24 hrs after addition of spermine at a lower concentration of 12.5 mM. While the columnar nature of the phase is evident, the observation of striations *perpendicular* to the tube axis is striking (compare Fig. 2 b–d to the MT bundle in 2a with protofilaments parallel to the tubular axis). As we describe below, SAXS data shows that the striations comprising the ITT walls correspond to helical protofilaments.

To discover the transient structures, along the transition pathway from the B_{MT} to the B_{ITT} bundled phase, a series of samples at 12.5 mM spermine were maintained at 4 °C (in a water bath) and imaged at various times (30 min, 1 hr, 2 hrs, 5 hrs, 19 hrs) to capture early, early-to-intermediate, intermediate, and late time frames in the structural evolution between the bundled states (Fig. 3 a–k). At the very early stages of the transition from the B_{MT} phase (30 minutes post-addition of 12.5 mM spermine at 4 °C) with primarily MT bundles (B_{MT}) present, TEM shows the inside-out curling of PFs, often at the ends of the bundles and sometimes along the body of the bundle (Fig. 3 a–d and Supplementary Fig. S1). The diameter of the "pre-ring" curled PFs range from as small as ≈ 28 nm (Fig. 3a) to as large as ≈ 45.1 nm (Fig. 3d) and 49.8 nm (see Supplementary Fig. S1 a–f for diameters of a collection of "pre-ring" structures). Thus, while many initial curling PFs have a smaller diameter than the fully formed PF-rings observed at later times (discussed below) there are also examples of larger diameters. The large variation in the diameter at this "pre-ring stage" may not be surprising because the curling PFs are highly dynamical and the TEMs capture a moment during the peeling process.

Fig. 3 e–k shows TEMs corresponding to later times along the transition at 4° C. TEMs after 1 hr and 2 hrs were qualitatively similar where MT bundles are seen to coexist with fully formed rings with *no hint of ITTs* (Fig. 3e, early-to-intermediate stage TEM at 2 hrs). Fig. 3 (f–i) shows intermediate stage TEMs of different regions of the same sample at 5 hrs where one can now see emerging short ITTs and ITT bundles (including an end-view of an ITT trimer in Fig. 3g) co-existing with rings, MTs and MT bundles. Further along at 19 hrs,

bundles of ITTs now dominate the structure at this late stage and fully formed bundles of ITTs are seen to co-exist with some rings, very few MTs and *no MT bundles* (Fig. 3j). It is interesting to note that while the micrograph in Fig. 3j shows a well-ordered bundle of ITTs, Fig. 3k shows a more rare region of the same sample at 19 hrs where short emerging ITTs (with a few rings around them) appear to merge and interact laterally. The diameters of the rings seen in TEMs (Fig. 3 e–k) are now seen to be comparable to the diameter of the ITTs (Fig. 3 f–k and Fig. 2 c, d). A notable observation in the TEM of Fig. 3k is that one can see that the assembling rings along the tubes have highly non-uniform diameters (see e.g. arrows pointing to different diameters along the tube), which becomes more uniform (Fig. 3j) once the ITTs are fully formed with the rings opening/fusing to form the helical PFs comprising the tubule wall (with the helical nature confirmed by SAXS). We do not expect the inside-out rings to further twist and expose another surface in the process of going from rings to the helical PFs, as this would result in a large elastic cost. Furthermore, the similarities in pitch and size between the single-walled tubule shown here and the outer layer of the previously observed double-layered tubule at 1.2 nm resolution[33] strongly suggest that the outer surface of the ITTs corresponds to the inner lumen of MTs.

Observations from TEMs, covering the early to intermediate to late and final stages of conversion of the B_{MT} phase to the B_{ITT} phase, indicate that the tubulin rings are the building blocks of the nascent ITTs. The formation of inside-out rings (Fig. 3 e) after the initial curling of PFs (Fig. 3 a–d) and *before* the emergence of B_{ITT} structures (Fig. 3 f–i), and their near absence in the B_{ITT} phase (Fig. 2d after 24 hrs at 4 °C; see also the B_{ITT} phase TEMs at RT after 10 days in Fig. 2 b, c), indicates that they have self-assembled, in the presence of cationic spermine, into the inverted tubulin tubules with the outer surface corresponding to the inside luminal surface of the MTs.

To further show that the rings are the building blocks of the ITTs we performed a comprehensive statistical analysis of the distribution in the ring diameters on a TEM of disassembling MT bundles, which showed a very large number of rings. Fig. 4 a–c shows TEMs where after 15 minutes at $T \approx 0$ °C (samples with 15 mM spermine immersed in ice) micrographs already show an intermediate regime with coexistence of MT bundles with short ITT bundles together with an abundance of tubulin rings surrounding the bundles and within bundles (see, e.g., arrow pointing to c-PFs in depolymerizing MT bundle in Fig. 4b). Fig. 4d shows a histogram (number of rings versus ring diameter) of 1439 rings taken from a large area surrounding the region shown in Fig. 4a (see full size TEM in Supplementary Fig. S2). The mean ring diameter is 38.6 nm with a standard deviation of 4.9 nm. We now see that the mean diameter of the inverted tubulin tubules observed in the TEMs (Fig. 2 c, d and Fig. 3 f–k) is *within the measured standard deviation (± 4.9 nm) in the mean diameter of the 1439 rings*. The size measurements from TEM agree well with the analysis of the x-ray SAXS data, which shows that the diameter of ITTs in solution (with no distortions) is on average 40.2 nm (the TEM data is for samples under vacuum, which invariably leads to some level of distortions).

In order to gain quantitative insight into the Angstrom-level structure of the inverted tubulin tubules (ITTs), and the kinetics of the structural evolution from the B_{MT} to the B_{ITT} phase, we carried out a series of synchrotron SAXS studies of taxol-stabilized MTs at various

spermine concentrations and over short and long times. The lower two profiles in Fig. 5a show synchrotron SAXS intensity as a function of the magnitude of the scattering wavevector q at RT for MTs and MT bundles (labeled B_{MT}) in the presence of 5 mM spermine 10 days after bundle formation. After background subtraction (see Methods), the scattering from MTs can be quantitatively fit to $|F_{MT}|^2 \propto |[\sin(q_z L/2)/q_\perp q_z]^* [(R_{in}+w)J_1(q_\perp(R_{in}+w))-R_{in}J_1(q_\perp R_{in})]|^2$, averaged over all orientations in q-space (Fig. 5b, MT, solid line through data, open circles). Here, F_{MT} is the x-ray form factor of a hollow cylinder with an inner radius $R_{in} = 80$ Å, a wall thickness $w = 49$ Å, and length much larger than R_{in} (over 1000 nm)[21,22,34,35]. ($q_\perp$, q_z are wave-vectors perpendicular and parallel to the tubular axis, respectively, and J_1 is the Bessel function of order 1.) The measured dimensions are consistent with high-resolution models of MTs with an average of 13 protofilaments[13].

The diffraction peaks of the B_{MT} phase (Fig. 5a) can be indexed to MTs arranged on a hexagonal lattice with a center-to-center distance $a_H = 4\pi/\sqrt{3}q_{10}$. This results in diffraction peaks at q_{10}, $q_{11} = \sqrt{3}q_{10}$, $q_{21} = \sqrt{7}q_{10}$, and $q_{31} = \sqrt{13}q_{10}$. (The q_{20}, q_{30}, and q_{22} peaks are close to the minima of the MT form factor and appear as weak peaks.) The background subtracted SAXS data for unoriented MT bundles (Fig. 5b, B_{MT}, open circles) is well fit by the MT form factor multiplied by the structure factor and averaged over all orientations in q-space (Fig. 5b, B_{MT}, solid line). Following previous work the structure factor peaks at each reciprocal lattice vector $\mathbf{G}_{hk}$ were modeled as squared Lorentzians, $[A_{hk}/(\kappa^2 + (q_\perp - G_{hk})^2)]^2$, with G_{hk}, amplitudes A_{hk} and a single peak width proportional to κ, as fitting parameters[22]. The non-linear least-squares fit of the model to the SAXS data gives $a_H = 28.7$ nm and $\kappa = 0.0041$ Å^{-1}, which leads to an average bundle width $L \approx 2(\pi\ln4)^{0.5}/\kappa = 101.3$ nm, corresponding to an average of ≈ 3.5 MTs (see Methods).

For MT bundles at 15 mM spermine the SAXS data after 10 days at RT (Fig. 5a) now shows evidence of coexistence of the bundled B_{MT} phase with the new B_{ITT} phase (arrow points to 1st order diffraction peak of the B_{ITT} phase). At 30 mM spermine the entire sample is in the B_{ITT} phase after 10 days at RT (Fig. 5a).

As mentioned earlier, the B_{MT} to B_{ITT} structural transformation at a constant spermine concentration is observed to occur at a greatly increased rate with decreasing temperature. At 2.5 ± 1.5 °C, MTs bundled with 2.5 mM spermine (where the B_{MT} phase is stable for more than 10 days at RT) are observed to have undergone the transition to the B_{ITT} phase after 12 hours (Fig. 5a and 5b, top profiles). The data range from q values less than 0.1 nm^{-1} to a q of 1.4 nm^{-1}, covering length scales from greater than 62 nm to 4.5 nm. For the low q range between 0.1 nm^{-1} and 1.0 nm^{-1} twelve Bragg peaks are clearly visible (Fig. 5b) and can be indexed to a 2D hexagonal lattice.

A quantitative fit of the data to a model scattering curve after background subtraction (Fig. 5b, top profile, black line) shows that the B_{ITT} phase consists of hexagonal bundles of helices. The model consisted of $|F_{finite\ size\ helix}|^2$ (where $F_{finite\ size\ helix}$ is the form factor of a finite size helical tubulin-oligomer) multiplied by a Lorentzian squared structure factor (as described for the B_{MT} phase) and averaged over all orientations in q space. For an infinitely long continuous helix oriented along the z-helical axis F_{helix} is proportional to Bessel functions of order n, $J_n(q_\perp R)$, located on discrete layer lines at $q_z = 2\pi n/P$, where n is an

integer, P is the helical pitch, and R is the radius of the helix[36]. To take into account both the finite length of the helix and the thickness of tubulin we used:

$$|F_{\text{finite size helix}}|^2 \propto \Sigma n |J_n(q_\perp R)|^2 * exp\left[-(q_z - 2\pi n/P)^2 L_z^2/4\pi\right] * exp\left[-\left(q_\perp^2 + q_z^2\right) R_g^2/2\right]$$

The first Gaussian function is Warren's approximation accounting for the finite length of the helix $L_z = NP$ (where N is the number of turns in the helix) and replaces the delta function peaks defining the discrete layer lines $q_z = 2\pi n/P$ for an infinite helix[37]. The second Gaussian term takes into account the finite cross-sectional size of the helical tubulin (i.e. the thickness of tubulin). Here, R_g is the radius of gyration of the cross-section of the helical tubulin[38].

The B_{ITT} SAXS data is dominated by the n = 0 line for the lower q data (< 1 nm^{-1}) and the n = 1 line for the higher q data (> 1 nm^{-1}). Fits of the data over the entire q range to the model (Fig. 5b, top profile, solid curve) gave a center-to-center distance of 45.6 nm for the inverted tubules. The bundle width inversely proportional to the width of the peaks was L ≈ $2(\pi \ln 4)^{0.5}/\kappa = 261$ nm, which corresponds to an average of 5.7 helices. The fit also gave R = 20.2 nm for the radius of the helical PFs (i.e. obtained from the zeros of $J_0(q_\perp R)$) consistent with the TEM of inverted tubulin tubules (Fig. 2 b–d and Fig. 3j)).

The helical character of the tubulin oligomers, comprising the wall of the inverted tubulin tubule seen in TEM (Fig 2 b–d and Fig. 3j), is established unambiguously by the high quality of the fit of the model to the data in the higher q range (1.15 nm^{-1} < q < 1.4 nm^{-1}) where the helical form factor $|F_{\text{finite size helix}}|^2$ is now dominated by the n = 1 term (Fig. 5c, expanded view, data are open circles, solid line is fit to the helical model). The peak positions in the scattering data correspond precisely to the n = 1 layer Bessel Function $J_1(q_\perp R)$ and gave a pitch of 5.29 nm with R = 20.2 nm. The best fit also yielded a physical radius of the tubulin cross-section (i.e. the thickness of tubulin)[38], Rtubulin = $2 R_g \approx 2.12$ nm close to electron microscopy data (≈ 2.5 nm) on tubulin[13], and an average helix height $L_z \approx 317$ nm (∞ inverse width of the high q peaks of Fig. 5c). If we fixed R_g at 1.77 (i.e. Rtubulin = 2.5 nm) the quality of the fit was only slightly inferior indicating that R_{tubulin} could not be determined better than ± 0.2 nm.

We compared this helical model to a model of stacked rings of protofilaments, which gave a poor fit. For this latter model a 1D structure factor along the stacking direction $S(q_z) = A exp[(q_z - 2\pi/d)^2 L_z^2/4\pi]$ was multiplied by $|F_{\text{Ring}}|^2 \propto |[\sin(q_z T/2)/q_\perp q_z] * [(R_{in}+w)J_1(q_\perp(R_{in}+w)) - R_{in}J_1(q_\perp R_{in})]|^2$, and orientationally averaged[38]. Here, F_{Ring} is the form factor of a ring with inner radius R_{in}, thickness T (i.e. along the stacking direction) and width w. The dotted line in Fig. 5c, which is not able to predict the correct peak positions, is the best fit of the data to the stacked-ring model (with d = 5.29 nm, T = 50 Å, w = 4.9 nm, R_{in} = 17.7 nm (consistent with R = R_{in} + w/2 = 20.2 nm determined by the minima in the low q data), and L_z = height of stacked rings = 343 nm). The chiral columnar nature of the B_{ITT} phase makes it closely analogous to the chiral discotic phases of thermotropic liquid crystals[39,40].

To gain further insight into the nature of this novel phase change driven by a conformational change in the tubulin subunit we have quantitatively characterized the kinetics of the B_{MT} to B_{ITT} transition. Samples in the B_{MT} phase were rapidly cooled to $\approx 0°$ C (via a x-ray sample holder in thermal contact with a water bath) and SAXS was used to follow their evolution over short time scales of order one to two hours (Fig. 6a). The gradual transformation of the B_{MT} phase to the B_{ITT} phase shows that there are significant energy barriers separating these phases. Assuming the bundle diameter within a given phase does not significantly change, the amplitude of each peak is proportional to the number of bundles in that phase[41]. The (10) peak amplitudes are plotted as a function of time, t, in Fig. 6b and fit to a simple model of the transition kinetics. The destruction of the B_{MT} phase was fit to a model assuming a constant rate of disassembly, $R(B_{MT})$. Thus, the amplitude of the (10) peak of the B_{MT} phase was assumed to be proportional to $\exp(-R(B_{MT})t)$. The amplitude of the (10) peak of the B_{ITT} phase was fit to a function proportional to $\{1-\exp[-R(B_{ITT})t]\}$ with $R(B_{ITT})$ a constant rate of assembly of the B_{ITT} phase. If the B_{MT} phase decayed directly into the B_{ITT} phase than $R(B_{ITT}) = R(B_{MT})$, otherwise they are not equal. For example, for 15 mM spermine (Fig. 6a) fits to the data gave $R(B_{MT}) = 0.5 \pm 0.1$ hr^{-1} and $R(B_{ITT}) = 2.0 \pm 0.2$ hr^{-1} indicating that there is at least one intermediate state between the two phases. As described earlier TEM micrographs of samples transitioning from the B_{MT} to the B_{ITT} phase show that the B_{MT} phase disassembles into inside-out curling PFs with PF-rings self-assembling (in the presence of spermine) into the B_{ITT} phase. Thus, the transition between the two condensed phases occurs through a non-tubular intermediate.

The transformation of the B_{MT} phase, first to curved oligomers, and then to the B_{ITT} phase involves overcoming two energy barriers with corresponding time scales $1/R(B_{MT})$ and $1/R(B_{ITT})$. The rate limiting step in the disassembly of the B_{MT} phase to curved tubulin oligomers, in the presence of spermine, is presumably the rupture of the inter-protofilament bonds[12], while the kinetic barrier for the conversion of tubulin oligomers to helical columns may be due to the electrostatic repulsion between anionic oligomers (which is counter-acted by cationic spermine). We have measured $R(B_{ITT})$ and $R(B_{MT})$ as a function of spermine concentration with SAXS (Fig. 6c) and found the rates increase with spermine concentration. This finding establishes that spermine concentration modulates the barrier height between the straight and curved conformations of taxol-stabilized protofilaments, because the rate of disassembly, $R(B_{MT})$, which increases with spermine concentration, is proportional to $\exp(-\Delta E/k_B T)$, where ΔE is the energy barrier and k_B is the Boltzmann constant. It further suggests that spermine enhances the association of c-PFs into helices.

We note that the disassembly of taxol-stabilized MTs in the B_{MT} phase, due to lowering of the straight-to-curved energy barrier, is specific and occurs with spermine and not with spermidine or oligolysine on the time scales of two to three weeks studied in this paper (even at $T \approx$ a few degrees °C where spermine disassembles the B_{MT} phase in hours). However, the assembly of tubulin rings (i.e. GDP-tubulin in the absence of taxol and GTP) into the B_{ITT} phase is non-specific and also occurs with other oligolysine (+5) and spermidine (+3) (see Supplementary, Fig. S3).

The work described here shows that spermine controls the straight to curved transition rate in taxol-stabilized GDP-protofilaments. This has led to the creation of microtubule bundles,

which upon a spermine trigger, undergo a dynamical transformation to an assembly of inverted tubulin tubules. The creation of such robust assemblies where the "inner lumen" of MTs is stably exposed allows for a convenient platform for future experiments addressing interactions of biomolecules with the inner surface of MTs. Important examples of such molecules include, MT-associated-protein tau (implicated in certain neurodegenerative diseases[42–44]), which has been hypothesized to have a MT inner lumen binding site (in addition to binding sites on the outer surface of MTs)[45,46], and cancer chemotherapy drugs targeting the MT inner lumen[16–19]. More generally this work opens the path for a new paradigm for nanoscale assembly, which incorporates biological building blocks with "pre-programmed & triggerable" shape evolving property. Due to their inherent encoded properties many enzymes (similar to tubulin GTPase employed in the current work) would provide natural choices for building blocks of assemblies, which would disassemble on demand and reassemble the shape-remodeled building blocks into a different structure with distinct function. Novel applications may include encapsulation of molecules, in the initial structure, and release upon triggered disassembly.

Methods

Sample Preparation

Purified tubulin was obtained from MAP-rich bovine brain MT protein as described by Miller and Wilson[47]. MTs were polymerized from tubulin at 4 mg/ml in 50 mM PIPES, pH 6.8, 1 mM $MgCl_2$, 1mM EGTA, 1mM GTP, and 5% glycerol by incubating in a 37 °C water bath for 20 min. The MTs were then stabilized by the addition of 20μM taxol. The taxol-stabilized MTs were then sedimented through a sucrose cushion (to remove unpolymerized tubulin) and resuspended (to 4 mg/ml tubulin) with 20μM taxol-PEM_{50} buffer. The final concentration for all TEM samples was 2 mg/ml tubulin and 10 μM taxol (taxol/tubulin molar ratio = 0.55) after dilution by half by mixing equal volumes of MT and spermine (prepared using Millipore H_2O (18.2 MΩ)). Just before TEM was performed the samples were diluted to 0.2 mg/ml at the desired spermine concentration and immediately imaged. We also checked selected TEM samples where the sucrose cushion step (i.e. to remove unpolymerized tubulin) was not performed. For these samples, TEMs depicting the early stage outwardly curling of PFs leading to MT depolymerization are unchanged (compare Figs. 3 (a,d) to (b,c)). However, in addition to the new inverted tubulin tubules described in the paper we also observe co-existence with double walled tubule structures (see Supplementary Fig. S4). These double walled structures are not observed when the sucrose cushion step is employed. Previous studies have reported on similar double-walled structures obtained along a different pathway in mixtures of tubulin and cationic macromolecules[27–30].

Samples for transmission electron microscopy experiments were prepared as follows. Highly stable Formvar carbon coated copper grids (Ted Pella) were loaded with sample and the excess solution was wicked off with Watmann paper, 1 wt% Uranyl Acetate was added for 20 sec, wicked off, and then washed with 5 drops of Millipore H_2O (18.2 MΩ). Unless otherwise noted the samples were allowed to dry overnight before measurements. The x-ray samples were prepared by centrifuging the 2 mg/ml tubulin and 10 μM taxol preparations

(with the various concentrations of spermine as noted in the text) at 16,000 g for one hour. The pellets and supernatants were transferred to 1.5 mm quartz capillaries and sealed with flame. The taxol-stabilized MTs used in the x-ray studies employed the sucrose cushion step to remove unpolymerized tubulin.

X-ray scattering

Small angle x-ray scattering experiments were performed at beamline 4–2 of the Stanford Synchrotron Radiation Laboratory at 8.98 keV. Data analysis was done by incorporating the structure factors and form factors described in the text into widely available non-linear least squares fitting routines and independently in program X+[48,49]. The background subtracted from the raw SAXS data consisted of a polynomial that passed through the scattering minima of the SAXS data[21,22,34,35]. The width of the bundles in the B_{MT} and B_{ITT} phases were determined by matching the Lorentzian squared structure factor ($[A_{hk}/(\kappa^2 + (q_\perp - G_{hk})^2)]^2$) at $|q_\perp - G_{hk}| = \kappa$ (with intensity at ¼ of the maximum) to a Warren-type Gaussian line-shape proportional to $\exp(-|q_\perp - G_{hk}|^2 L^2/4\pi)$ describing a lattice with domain size L (also with intensity at ¼ of the maximum)[37]. This procedure leads to an average bundle width $L \approx 2(\pi\ln4)^{0.5}/\kappa = 4.17/\kappa$. Alternatively, one may obtain the proportionality between L and $1/\kappa$ (which is proportional to the bundle width) by independently fitting the data either to a Lorentzian squared or a Warren-type Gaussian (which does not fit as well as a Lorentzian squared) and directly comparing L and $1/\kappa$. This procedure yields $L \approx 3.8/\kappa$ (which is within 10% of the former procedure).

Electron Microscopy

Transmision experiments were performed at 80 kV in a JEM 1230 (JEOL) instrument at the University of California at Santa Barbara (Fig. 2 a–c, Fig. 4 a–c, and Fig. S2) and at 300 kV in a JEM-3011HR (JEOL) electron microscope in the National Nanofab Center at KAIST (Fig. 2d, Fig. 3, Fig. S1, and Fig. S4).

Supplementary Material

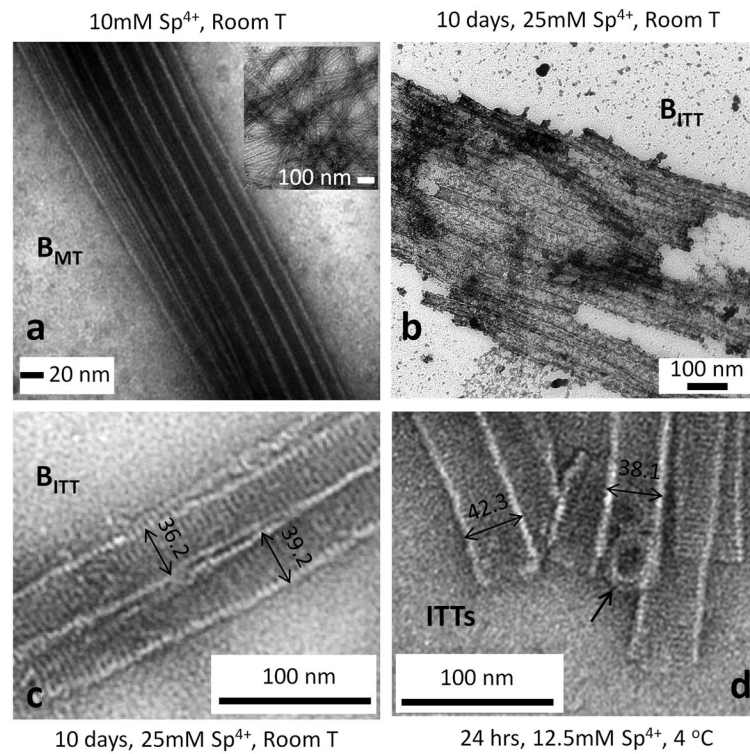Refer to Web version on PubMed Central for supplementary material.

Acknowledgements

References

1. Bray, D. Cell Movements: From Molecules to Motility. 2. Garland; New York: 2001.

2. Thomas, TD.; Earnshaw, WC.; Lippincott-Schwartz, J. Cell Biology. 2. Saunders, Elsevier; Philadelphia: 2008.

3. Israelachvili, JN. Intermolecular & Surface Forces. Academic Press; Waltham: 1992.

4. Sackmann E. Membrane Bending Energy Concept of Vesicle-Shape and Cell-Shape and Shape-Transitions. Febs. Letters. 1994; 346:3–16. [PubMed: 8206154]

5. Chiruvolu S, et al. A Phase of Liposomes with Entagled Tubular Vesicles. Science. 1994; 266:1222–1225. [PubMed: 7973704]

6. Zidovska A, et al. Block Liposomes from Curvature-Stabilizing Lipids: Connected Nanotubes, -rods and -spheres. Langmuir. 2009; 25:2979–2985. [PubMed: 18834165]

7. Zidovska A, et al. Block Liposome and Nanotube Formation is a General Phenomenon of Membranes Containing Multivalent Lipids. Soft Matter. 2011; 7:8363–8369. [PubMed: 22707975]

8. Seeman NC, Belcher AM. Emulating biology: building nanostructures from the bottom up. Proc. Natl. Acad. Sci. U.S.A. 2002; 99:6451–6455. [PubMed: 11880609]

9. Ringler P, Schulz GE. Self-assembly of proteins into designed networks. Science. 2003; 302:106–109. [PubMed: 14526081]

10. Seeman NC. DNA in a material world. Nature. 2003; 421:427–431. [PubMed: 12540916]

11. Chworos A, et al. Building programmable jigsaw puzzles with RNA. Science. 2004; 306:2068–2072. [PubMed: 15604402]

12. Nogales E, Wang HW, Niederstrasser H. Tubulin rings: which way do they curve. Curr. Opin. Struct. Biol. 2003; 13:256–261. [PubMed: 12727521]

13. Lowe J, Li H, Downing KH, Nogales E. Refined structure of alpha beta-tubulin at 3.5 A resolution. J. Mol. Biol. 2001; 313:1045–1057. [PubMed: 11700061]

14. Ravelli RBG, et al. Insight into tubulin regulation from a complex with colchicine and a stathmin-like domain. Nature. 2004; 428:198–202. [PubMed: 15014504]

15. Mandelkow EM, Mandelkow E, Milligan RA. Microtubule Dynamics and Microtubule Caps: A Time-Resolved Cryo-Electron Microscopy Study. J. Cell Bio. 1991; 114:977–991. [PubMed: 1874792]

16. Nogales E, Wolf SG, Khan IA, Luduena RF, Downing KH. Structure of tubulin at 6.5 Å and location of the taxol-binding site. Nature. 1995; 375:424–427. [PubMed: 7760939]

17. Mitra A, Sept D. Taxol allosterically alters the dynamics of the tubulin dimer and increases the flexibility of microtubules. Biophys. J. 2008; 95:3252–3258. [PubMed: 18621813]

18. Jordan MA, Wilson L. Microtubules as a target for anticancer drugs. Nature Reviews Cancer. 2004; 4:253–265. [PubMed: 15057285]

19. Jordan, MA.; Wilson, L. Cancer Drug Discovery and Development, The Role of Microtubules in Cell Biology, Neurobiology, and Oncology. Fojo, T., editor. Humana Press; New York: 2008. p. 47-81.

20. Elie-Caille C, et al. Straight GDP-tubulin protofilaments form in the presence of taxol. Curr. Biol. 2007; 17:1765–1770. [PubMed: 17919908]

21. Choi MC, et al. Human microtubule-associated-protein tau regulates the number of protofilaments in microtubules: a synchrotron x-ray scattering study. Biophys. J. 2009; 97:519–527. [PubMed: 19619466]

22. Needleman DJ, et al. Higher-order assembly of microtubules by counterions: From hexagonal bundles to living necklaces. Proc. Natl. Acad. Sci. U.S.A. 2004; 101:16099–16103. [PubMed: 15534220]

23. Gelbart WM, Bruinsma RF, Pincus PA, Parsegian VA. DNA-inspired electrostatics. Physics Today. 2000; 53:38–44.

24. Koltover I, Wagner K, Safinya CR. DNA condensation in two dimensions. Proc. Natl. Acad. Sci. U.S.A. 2000; 97:14046–14051. [PubMed: 11121015]

25. Manning GS. Limiting Laws and Counterion Condensation in Polyelectrolyte Solutions I. Colligative Properties. J. Chem. Phys. 1969; 51:924–933.

26. Savarin P, et al. Central role for polyamines in microtubule assembly in cells. Biochemical J. 2010; 430:151–159.

27. Jacobs M, Bennett PM, Dickens MJ. Duplex microtubule is a new form of tubulin assembly induced by polycations. Nature. 1975; 257:707–709. [PubMed: 1186848]

28. Erickson HP, Voter WA. Polycation-induced assembly of purified tubulin. Proc. Natl. Acad. Sci. U.S.A. 1976; 73:2813–2817. [PubMed: 1066692]

29. Kuznetsov SA, Gelfand VI, Rodionov VA, Rosenblat VA, Gulyaeva JG. FEBS Lett. 1978; 95:343–346. [PubMed: 102536]

30. Erickson, HP. Cell Motility. Goldman, R.; Pollard, T.; Rosenbaum, J., editors. Cold Spring Harbor; 1976.

31. Howard WD, Timasheff SN. GDP state of tubulin: stabilization of double rings. Biochemistry. 1986; 25:8292–8300. [PubMed: 3814585]

32. Nicholson WV, Lee M, Downing KH, Nogales E. Cryo-electron microscopy of GDP-tubulin rings. Cell Biochem. Biophys. 1999; 31:175–183. [PubMed: 10593258]

33. Wang H-W, Nogales E. Nucleotide-dependent bending flexibility of tubulin regulates microtubule assembly. Nature. 2005; 435:911–915. [PubMed: 15959508]

34. Raviv U, et al. Cationic liposome-microtubule complexes: Pathways to the formation of two-state lipid-protein nanotubes with open or closed ends. Proc. Natl. Acad. Sci. U.S.A. 2005; 102:11167–11172. [PubMed: 16055561]

35. Raviv U, et al. Microtubule protofilament number is modulated in a stepwise fashion by the charge density of an enveloping layer. Biophys. J. 2007; 92:278–287. [PubMed: 17028134]

36. Cochran W, Crick FHC, Vand V. The stucture of synthetic polypeptides. I. The transform of atoms on a helix. Acta Crystal. 1952; 5:581–586.

37. Warren BE. X-Ray Diffraction in Random Layer Lattices. Phys. Rev. 1941; 59:693–698.

38. Glatter, O.; Kratky, O., editors. Small Angle X-ray Scattering. Academic Press Inc.; Waltham: 1982. p. 155

39. Levelut A. Structure of a disk-like mesophase. J. de Physique. 1979; 40:8184–8188.

40. Safinya CR, Liang KS, Varady WA, Clark NA, Andersson G. Synchrotron x-ray study of the orientational ordering D2-D1 structural phase transition of freely suspended discotic strands in triphenylene-hexa-dodecanoate. Phys. Rev. Lett. 1984; 53:1172–1175.

41. Guinier, A. Diffraction in Crystals, Imperfect Crystals, and Amorphous Bodies. Dover: 1963. X-Ray.

42. Goedert M, Spillantini MG. A Century of Alzheimer's Disease. Science. 2006; 314:77–781.

43. Roberson ED, Mucke L. 100 Years and counting: prospects for defeating Alzheimer's disease. Science. 2006; 314:781–784. [PubMed: 17082448]

44. Morris M, Maeda S, Vossel K, Mucke L. The Many Faces of Tau. Neuron. 2011; 70:410–426. [PubMed: 21555069]

45. Kar S, Fan J, Smith MJ, Goedert M, Amos LA. Repeat motifs of tau bind to the insides of microtubules in the absence of taxol. EMBO J. 2003; 22:70–77. [PubMed: 12505985]

46. Makrides V, Massie MR, Feinstein SC, Lew J. Evidence for two distinct binding sites for tau on microtubules. Proc. Natl. Acad. Sci. U.S.A. 2004; 101:6746–6751. [PubMed: 15096589]

47. Miller HP, Wilson L. Preparation of Microtubule Protein and Purified Tubulin from Bovine Brain by Cycles of Assembly and Disassembly and Phosphocellulose Chromatography. Meth. Cell Biol. 2010; 95:2–15.

48. Szekely P, Ginsburg A, Ben Nun T, Raviv U. Solution X-Ray Scattering Form Factors of Supramolecular Self-Assembled Structures. Langmuir. 2010; 26:13110–13129. [PubMed: 20695550]

49. Ben Nun T, Ginsburg A, Szekely P, Raviv U. X+: A Comprehensive, Computationally Accelerated, Structural Analysis Tool of Solution X-ray Scattering from Supramolecular Self-Assemblies. J. Appl. Cryst. 2010; 43:1522–1531.
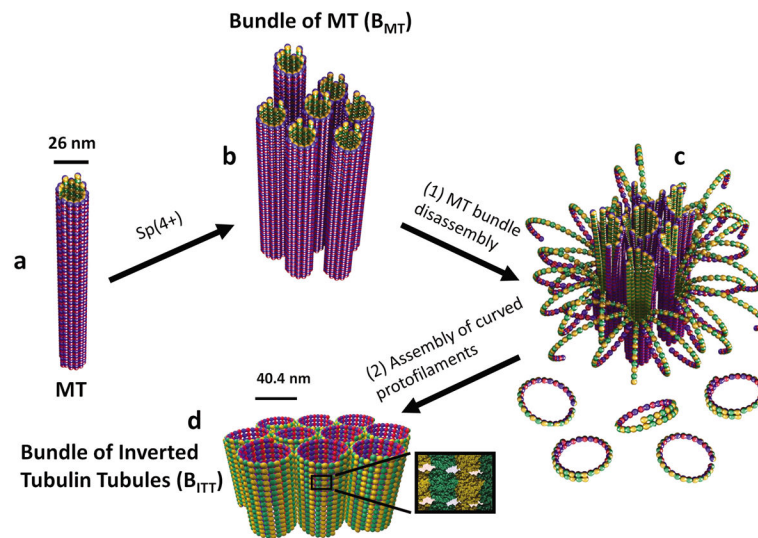
Figure 1. Schematic of a spermine (4+)-induced inversion process from bundles of taxol-stabilized microtubules (B_{MT}) to bundles of inverted tubulin tubules (B_{ITT})

a and **b**, Taxol-stabilized microtubules (MTs, **a**) may be induced to form MT bundles above a critical concentration of spermine (4+) counterions (B_{MT}, **b**). The bundles result from the nonspecific electrostatic attraction between spermine coated MTs. **c** and **d**, For concentrations several times larger than the critical bundling concentration a specific spermine-triggered straight-to-curved conformation transition in protofilaments, leads to MT disassembly into curved protofilaments (c-PFs) within the bundles (**c**). Concurrent to MT disassembly spermine counterions induce non-specific assembly of c-PFs into the B_{ITT} phase (**d**). Both phases are hierarchically ordered, liquid crystalline nanotubes, but the tubes are inverted: the tubulin surface, which is on the inside of the tubes in the B_{MT} phase is on the outside in the B_{ITT} phase.

10mM Sp^{4+}, Room T   10 days, 25mM Sp^{4+}, Room T

10 days, 25mM Sp^{4+}, Room T   24 hrs, 12.5mM Sp^{4+}, 4 °C

Figure 2. TEM of taxol-stabilized microtubule bundles (B$_{MT}$) and the new spermine-induced phase of bundles of inverted tubulin tubules (B$_{ITT}$)

a, A typical transmission electron microscopy (TEM) image of a taxol-stabilized microtubule bundle (10 mM spermine, room T) showing striations parallel to the cylinder axis due to the protofilaments. The bundle phase is dominant for less than 10 days. **Inset**, Taxol-stabilized microtubules with straight protofilaments. **b** and **c**, An example of a large bundle of inverted tubulin tubules (**b**, B$_{ITT}$) and a higher magnification of a smaller B$_{ITT}$ (**c**) where protofilaments appear as striations perpendicular to the cylinder axis. TEMs are for 25 mM spermine mixed with taxol-stabilized MTs and imaged after 10 days at room T. **d**, Example of the B$_{ITT}$ phase formed 24 hours after addition of 12.5 mM spermine at 4 °C. Arrow points to overlapping protofilament rings. In this sample preparation a sucrose cushion to remove unpolymerized tubulin (which was used for TEM samples (**a–c**)) was not employed and inverted tubulin tubules depicted here co-exist with double-walled structures shown in Supplementary Fig. S4 (see Sample Preparation in the Methods section). All TEMs were at taxol/tubulin molar ratio = 0.55.
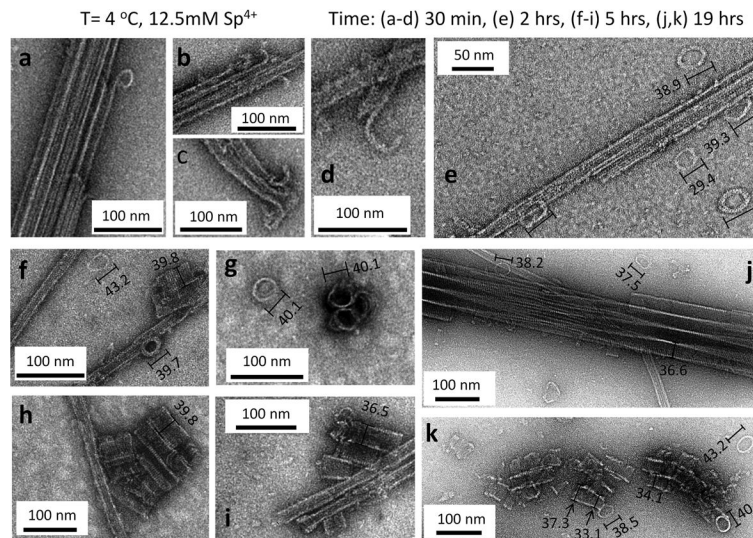
Figure 3. Time-dependent TEM of the pathway of inversion of taxol-stabilized microtubule bundles (B_{MT}) into bundles of inverted tubulin tubules (B_{ITT}) at 4 °C and 12.5 mM spermine
**a–d**, Transmission electron microscopy (TEM) of early stages of microtubule (MT) bundle disassembly at 30 minutes showing the inside-out curling of protofilaments (PFs) into "pre-ring" structures with a large variation in their diameters (see Supplementary Fig S1). This stage corresponds to Fig. 1c. **e**, Early-to-intermediate stage TEMs at 2 hrs show the presence of fully formed rings surrounding MT bundles, which dominate the phase at this early-to-intermediate stage where the inverted tubulin structure has not yet formed. TEMs at 1 hr show similar structures. **f–i**, Intermediate stage TEMs at 5 hrs showing short inverted tubulin tubules (ITTs) and ITT bundles (including an end view of an ITT trimer in **g**) co-existing with rings, MTs, and MT bundles. **j**, Late stage TEM at 19 hrs show fully formed bundles of ITTs and few isolated MTs and rings during this late stage. (In the final stage, in the B_{ITT} phase, no remaining MTs (and extremely few rings) are found as seen in Fig. 2 both at room T (Fig. 2 b, c) and at 4 °C 24 hrs post addition of 12.5 mM spermine (Fig. 2d).) **k**, A TEM of a different region of the same sample as in (j) at 19 hrs showing a rare region where short ITTs appear to be forming from the assembly of rings. The variation in the diameter of assembled rings is visible during ITT formation as discussed in the text. The rings in (**e–k**) have diameters ≈ the diameter of the ITTs. In the measurement of ring size the longer axis was taken because tilts in the ring make it appear as elliptical with the longer axis being a closer estimate of the true diameter. The sample preparations for TEMs (**b, c** at 30 minutes) and (**e–k** at 2, 5, 19 hrs) employed a sucrose cushion to remove unpolymerized tubulin after taxol-stabilization of MTs. The sucrose cushion was not employed for TEM samples (**a, d** at 30 minutes) (see Sample Preparation in the Methods section). All TEMs were at taxol/tubulin molar ratio = 0.55.
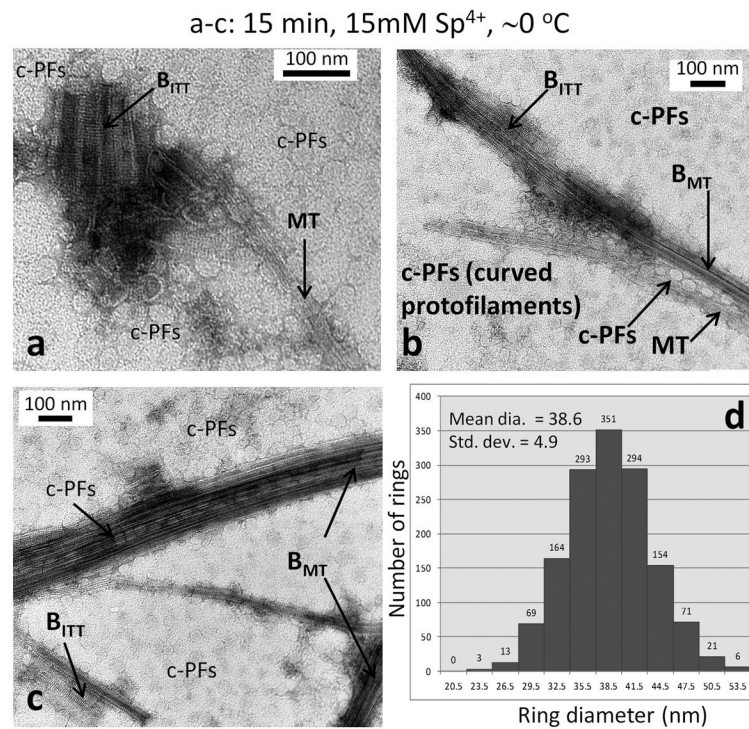
Figure 4. Size distribution of ring-like protofilaments in the coexistence regime of disassembling microtubule bundles (B_{MT}) and assembling bundles of inverted tubulin tubules (B_{ITT}) from TEM

a–c, Transmission electron microscopy (TEM) images (15 minutes after addition of 15 mM spermine at 0 °C) show coexistence of B_{MT} with short bundles of inverted tubulin tubules (B_{ITT}). Also seen are proliferation of ring-like curved protofilaments c-PFs, both in the vicinity of the bundled structures and within disassembling MT bundles (arrows pointing to c-PFs in (b) and (c)). **d**, Size distribution of 1439 rings in a larger part of the sample surrounding the region shown in the TEM in (**a**) (see Supplementary Fig. S2). The total number of rings in each box (with a width of 3 nm) is indicated at the top of each box. The mean size of 38.6 nm with a standard deviation of 4.9 nm for the rings is consistent with the diameter of ITTs ($\approx$ 40.4 nm) measured with SAXS of undistorted bundles of ITTs in solution. All TEMs were at taxol/tubulin molar ratio = 0.55.
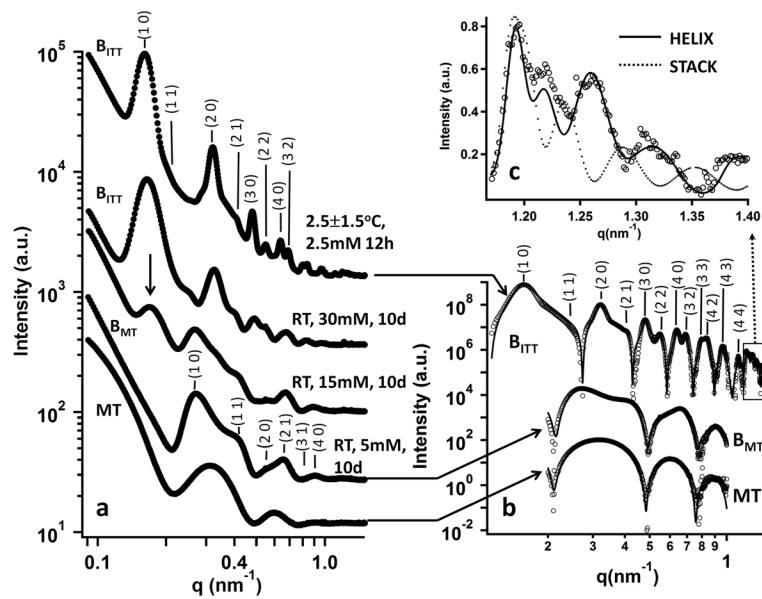
Figure 5. Synchrotron SAXS data of taxol-stabilized microtubule bundles (B_{MT}) and bundles of inverted tubulin tubules (B_{ITT})

a, Bottom profile shows synchrotron small-angle-x-ray-scattering (SAXS) data of taxol-stabilized microtubules (MT). The second through fourth profiles from bottom are SAXS data from room temperature samples taken 10 days after mixing increasing amounts of spermine with MTs: 5 mM spermine shows 2D hexagonal bundles of MTs (B_{MT}); 15 mM spermine shows coexistence of the B_{MT} phase with the new phase of bundles of inverted tubulin tubules (B_{ITT}, arrow points to first order diffraction peak); and 30 mM spermine shows the B_{ITT} phase. Top profile shows SAXS of the B_{ITT} phase formed at $\approx 2.5 \pm 1.5$ °C 12 hours after placing microtubules in the B_{MT} phase, with 2.5 mM spermine. **b**, Three scattering profiles from (**a**) (bottom two and top curves) after background subtraction with fitted model scattering curves (solid lines) as described in the text. Twelve peaks of the B_{ITT} phase can be indexed to a 2D hexagonal lattice. **c**, Expanded high q region showing comparison of scattering data to a model where the inverted tubulin columns consist of either helical protofilaments with a tight pitch (solid line, which fits the data well) or stacks of rings of curved protofilaments (dotted line, which does not fit the data). All samples were at taxol/tubulin molar ratio = 0.55.
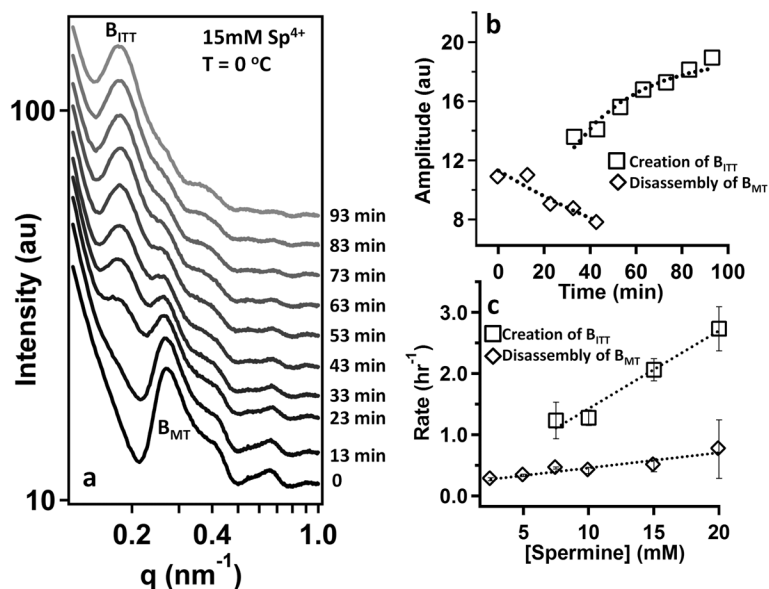
Figure 6. Time-dependent synchrotron SAXS data of the transition kinetics from bundles of microtubules (B_{MT}) to bundles of inverted tubulin tubules (B_{ITT})

a, The B_{MT} phase was suddenly taken from room temperature to $\approx 0°$ C and the resulting transition to the B_{ITT} phase was followed in real time (t) by synchrotron small-angle-xray-scattering (SAXS). The profiles are for SAXS scans of a sample with 15 mM spermine taken at the temperature change (t = 0), thirteen minutes after the temperature change, and subsequently every ten minutes. The scans are offset for clarity with t = 0 at the bottom and t = 93 minutes at the top. **b**, The amplitude of the (10) peak of the B_{MT} phase (open diamonds) and the B_{ITT} phase (open squares) obtained from best fits for the data in (**a**). For simplicity, the (10) peak of the coexisting B_{MT} and the B_{ITT} phases were fit to Gaussians. **c**, Rates of disassembly of the B_{MT} phase ($R(B_{MT})$, open diamond) and creation of the B_{ITT} phase ($R(B_{ITT})$, open squares) as a function of spermine concentration obtained from fits to SAXS data (as in (**a**) and (**b**) for 15 mM spermine). All SAXS samples were at taxol/tubulin molar ratio = 0.55.